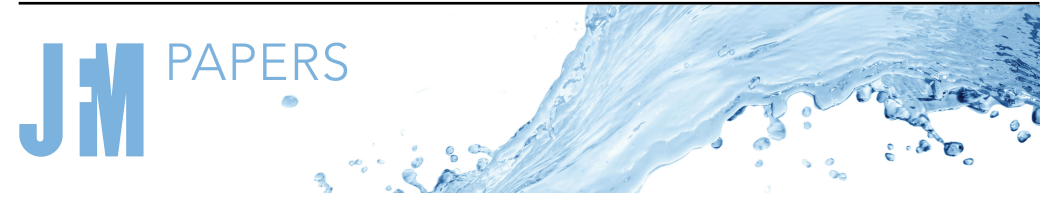
https://doi.org/10.1017/jfm.2025.10723 Published online by Cambridge University Press



Stability of plane Couette and Poiseuille flows rotating about the streamwise axis

Geert Brethouwer

Department of Engineering Mechanics, KTH Royal Institute of Technology, SE-10044 Stockholm, Sweden

Corresponding author: Geert Brethouwer, geert@kth.se

(Received 7 November 2024; revised 8 September 2025; accepted 16 September 2025)

We study the stability of plane Poiseuille flow (PPF) and plane Couette flow (PCF) subject to streamwise system rotation using linear stability analysis and direct numerical simulations. The linear stability analysis reveals two asymptotic regimes depending on the non-dimensional rotation rate (Ro): a low-Ro and a high-Ro regime. In the low-Ro regime, the critical Reynolds number Re_c and critical streamwise wavenumber α_c are proportional to Ro, while the critical spanwise wavenumber β_c is constant. In the high-Roregime, as $Ro \to \infty$, we find $Re_c = 66.45$ and $\beta_c = 2.459$ for streamwise-rotating PPF, and $Re_c = 20.66$ and $\beta_c = 1.558$ for streamwise-rotating PCF, with $\alpha_c \propto 1/Ro$. Our results for streamwise-rotating PPF match previous findings by Masuda et al. (J. Fluid Mech., vol. 603, 2008, pp. 189–206). Interestingly, the critical values of β_c and Re_c at $Ro \to \infty$ in streamwise-rotating PPF and PCF coincide with the minimum Rec reported by Lezius & Johnston (J. Fluid Mech., vol. 77, 1976, pp. 153–176) and Wall & Nagata (J. Fluid Mech., vol. 564, 2006, pp. 25–55) for spanwise-rotating PPF at Ro = 0.3366 and PCF at Ro = 0.5. We explain this similarity through an analysis of the perturbation equations. Consequently, the linear stability of streamwise-rotating PCF at large Ro is closely related to that of spanwise-rotating PCF and Rayleigh–Bénard convection, with $Re_c = \sqrt{Ra_c}/2$, where Ra_c is the critical Rayleigh number. To explore the potential for subcritical transitions, direct numerical simulations were performed. At low Ro, a subcritical transition regime emerges, characterised by large-scale turbulent-laminar patterns in streamwise-rotating PPF and PCF. However, at higher Ro, subcritical transitions do not occur and the flow relaminarises for $Re < Re_c$. Furthermore, we identify a narrow Ro range where turbulent-laminar patterns develop under supercritical conditions.

Key words: shear-flow instability, transition to turbulence, rotating turbulence

1. Introduction

Wall-bounded shear flows such as plane Poiseuille or channel flow (PPF) and plane Couette flow (PCF) subject to system rotation display many interesting physical phenomena, for example, turbulent–laminar patterns (Brethouwer, Duguet & Schlatter 2012; Brethouwer 2017), recurring bursts of turbulence (Brethouwer *et al.* 2014; Brethouwer 2016), large-scale structures (Gai *et al.* 2016; Brethouwer 2017), multiple states (Yang & Xia 2021) and strong increases in momentum and heat transfer (Brauckmann, Salewski & Eckhardt 2016; Brethouwer 2021, 2023). Studying the stability of such flows subject to system rotation in various directions may help to understand rotating shear flows in engineering applications.

The stability of PPF and PCF with and without spanwise system rotation has been studied extensively (see e.g. Hart 1971; Hung, Joseph & Munson 1972; Lezius & Johnston 1976; Schmid & Henningson 2001; Wall & Nagata 2006; Daly et al. 2014; Nagata, Song & Wall 2021). From now on, we abbreviate non-rotating PCF and PPF to NPCF and NPPF, respectively, and PCF and PPF subject to spanwise system rotation to ZPCF and ZPPF, respectively. The NPCF is linearly stable at any Reynolds number Re, whereas in NPPF two-dimensional Tollmien–Schlichting (TS) modes with $\beta=0$ are linearly unstable for $Re \geqslant 5772.3$ (Schmid & Henningson 2001). Here and in the following $Re = U_{cl}\delta/\nu$ for PPF and $Re = U_w\delta/\nu$ for PCF, where U_{cl} is the centreline velocity, U_w is the velocity of the two walls moving in opposite directions, δ is the half gap-width and ν is the viscosity. Subscript c is used to denote values at critical condition for linear instabilities. Further, α and β are the streamwise and spanwise wavenumbers, respectively, non-dimensionalised by δ .

Spanwise rotation can drastically reduce the critical Reynolds number Re_c of PPF. Lezius & Johnston (1976) and Alfredsson & Persson (1989) did a linear stability analysis (LSA) of ZPPF assuming two-dimensional perturbations with $\alpha=0$ and found that the minimum critical Reynolds number is $Re_c=66.40$ at $Ro_c=1/3$. Here and in the following $Ro=2\Omega\delta/U_{cl}$ for PPF and $Ro=2\Omega\delta/U_{w}$ for PCF, where Ω is the imposed system rotation rate. Wall & Nagata (2006) extended the LSA to three-dimensional perturbations and confirmed that at low Re, ZPPF is most unstable to perturbations with $\alpha=0$. They recomputed the critical values and found the lowest $Re_c=66.448$ at Ro=0.3366 with $\beta_c=2.459$.

Lezius & Johnston (1976) also pointed out the similarity between the linear perturbation equations of ZPCF and Rayleigh–Bénard convection between two flat plates. From that similarity follows $16Re_c^2Ro(1-Ro)=Ra_c$ and $\beta_c=3.117/2=1.558$ when Ro>0, where $Ra_c=1707.762$ is the critical Rayleigh number (Chandrasekhar 1961) and Ro>0 corresponds to anti-cyclonic rotation. The factors 16 and 2 in the relations for Re_c and β_c arise when the half-gap width δ is used for non-dimensionalisation instead of the gap width. The previous relation shows that the minimum $Re_c=20.6625$ of ZPCF occurs at Ro=0.5. The non-normality of the linearised Navier–Stokes operator of PPF and PCF can explain the strong reduction of Re_c by spanwise rotation (Jose & Govindarajan 2020).

Experiments (Alfredsson & Persson 1989; Tsukahara, Tillmark & Alfredsson 2010) show that streamwise vortices develop in ZPPF and ZPCF slightly above Re_c . The vortices are steady and turbulent motions are absent at these low Re, but the vortices become three-dimensional and unstable when Re increases (Yang & Kim 1991; Finlay 1992; Nagata 1998; Tsukahara $et\ al.\ 2010$; Daly $et\ al.\ 2014$; Nagata $et\ al.\ 2021$), and turbulence sets in at sufficiently high Re (Tsukahara $et\ al.\ 2010$; Salewski & Eckhardt 2015; Brethouwer 2017; Jose $et\ al.\ 2017$; Brethouwer 2021).

The effect of system rotation about axes other than the spanwise axis on PPF has also been investigated. Wu & Kasagi (2004) studied the effect of system rotation with various rotation axis directions on turbulent PPF using direct numerical simulation (DNS). The PPF subject to streamwise system rotation, abbreviated as XPPF, has also been investigated. Direct numerical simulation (Oberlack *et al.* 2006; Yang, Su & Wu 2010; Yang & Wang 2018; Yang *et al.* 2020; Yu *et al.* 2022; Hu *et al.* 2023, 2024) and experiments (Recktenwald *et al.* 2007) of turbulent XPPF show a secondary mean flow and distinct Taylor–Görtler vortices, which are inclined to the streamwise direction.

Instabilities in XPPF have been studied via LSA and nonlinear analysis by Masuda, Fukuda & Nagata (2008). They used a non-dimensional rotation rate $\Omega^* = 2\Omega \delta^2/\nu$, which can be related to Ro by noting that $\Omega^* = Re\ Ro$. Masuda $et\ al$. (2008) observed two asymptotic neutral stability regimes for three-dimensional perturbations in the LSA: one at low Ro with $Re_c = 33.923/Ro$, and one at high Ro with $Re_c = 66.45$ and $\beta_c \simeq 2.5$ and α_c decreasing with Ro. At very low Ro, XPPF is most unstable to two-dimensional TS modes. The values of Re_c and β_c in XPPF at high Ro are remarkably similar to the minimum $Re_c = 66.448$ and $\beta_c = 2.4592$ occurring at Ro = 0.3366 in ZPPF (Wall & Nagata 2006). Masuda $et\ al$. (2008) did not comment on this similarity, but we show that it is not a coincidence.

Linear stability analysis does not always accurately predict a critical Re for transition. Disturbances can exhibit transient energy growth in linearly stable flows due to the non-normality of the linearised Navier–Stokes operator (Grossmann 2000), potentially triggering a subcritical transition (Orszag & Patera 1980; Daviaud, Hegseth & Bergé 1992). Consequently, the energy method has been employed to determine an energy-based Reynolds-number threshold Re_E , below which all disturbances monotonically decay (Boeck, Brynjell-Rahkola & Duguet 2024). This approach has been applied to NPPF and NPCF (Orr 1907; Busse 1969, 1972; Joseph 1976; Falsaperla, Giacobbe & Mulone 2019), showing that Re_E in NPPF is two orders of magnitude lower than Re_c . However, even if transient growth occurs, a flow may relaminarise if disturbances do not grow sufficiently to trigger a subcritical transition. Hence, Re_E can be significantly lower than the critical Re below which a shear flow remains laminar (Fuentes, Goluskin & Chernyshenko 2022).

Although Re_E is a conservative measure, it is observed that turbulence can persist in NPPF at Re much lower than Re_c and in NPCF at finite Re. However, below some Re threshold, NPPF and NPCF are not uniformly turbulent but transitional. Intermittent turbulence, sometimes forming large-scale oblique bands with alternating laminar-like and turbulent-like flow, can develop in a range of Re (Duguet, Schlatter & Henningson 2010; Shimizu & Manneville 2019; Tuckerman, Chantry & Barkley 2020). The flows eventually become laminar at lower Re, regardless of the initial conditions, and fully turbulent at higher Re.

Subcritical transition has also been studied in rotating shear flows. Jose *et al.* (2017) investigated transient growth in ZPPF and showed that the critical Reynolds number for such growth is almost independent of Ro, decreasing from 51 at low rotation to 41 at high rotation. These values are far below Re_c , both for $Ro \leq 10^{-2}$ and for large Ro. Their DNS confirmed that subcritical transition can occur at low Ro. Also, DNS and experiments of ZPCF with cyclonic rotation show subcritical transition and turbulent–laminar patterns in some (Re, Ro) range (Tsukahara *et al.* 2010; Brethouwer *et al.* 2012).

Subcritical transition to turbulence in XPPF has not, to our knowledge, been examined in detail. The values of Ro considered in DNS of XPPF are $Ro \approx 0.1$ (Oberlack *et al.* 2006) and higher, where Re_c is much lower than the Re in the DNS, so the transition is supercritical. The energy and linear stability of spiral flow between concentric cylinders,

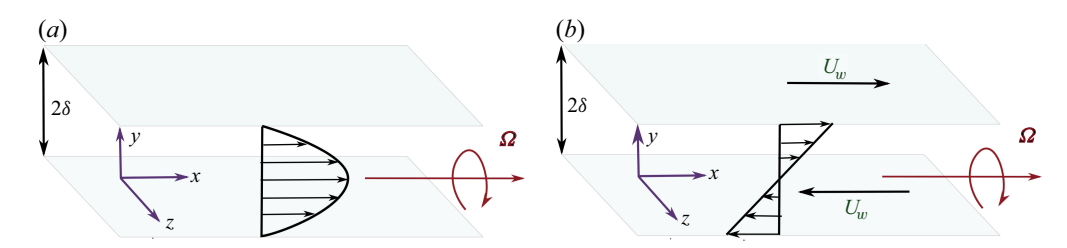


Figure 1. Configurations for (a) XPPF and (b) XPCF.

rotating and sliding relative to one another, with or without a uniform axial pressure gradient, have been investigated by Joseph & Munson (1970), Hung *et al.* (1972) and Joseph (1976). Both XPCF and XPPF represent two limiting narrow-gap cases of spiral flow with equal rotation rates of the inner and outer cylinders.

In summary, the stability of ZPPF and ZPCF has been extensively studied, whereas the stability of XPPF and XPCF has received much less attention. Only Masuda *et al.* (2008) and briefly Joseph & Munson (1970), Hung *et al.* (1972) and Joseph (1976) have studied these two flow cases. Many aspects of the behaviour of the critical modes as well as the potential of subcritical transition remain unclear. In this study, we investigate the stability of XPPF and XPCF with the aim of obtaining a deeper physical understanding of these flows. We perform both LSA and DNS to examine the possibility of subcritical transition.

2. Methodology: linear stability analysis and direct numerical simulations

2.1. Configuration and governing equations

We investigate the stability of viscous incompressible PCF and pressure-driven PPF subject to constant system rotation about the streamwise axis, i.e. XPCF and XPPF, as illustrated in figure 1. The streamwise, wall-normal and spanwise coordinates non-dimensionalised by the half-gap width δ are denoted by x, y and z, respectively, and the corresponding velocity components by u, v and w, respectively. The two infinite plane no-slip walls are at $y = \pm 1$. The velocity \boldsymbol{u} in the rotating frame of reference in both flow cases is governed by the non-dimensional Navier–Stokes equations:

$$\frac{\partial \mathbf{u}}{\partial t} + \mathbf{u} \cdot \nabla \mathbf{u} = -\nabla p + \frac{1}{Re} \nabla^2 \mathbf{u} - Ro(\hat{\mathbf{x}} \times \mathbf{u}), \quad \nabla \cdot \mathbf{u} = 0, \tag{2.1}$$

where \hat{x} is the unit vector in the x direction. The last term in the momentum equation is the Coriolis force and the centrifugal force is absorbed in a modified pressure p. The laminar streamwise velocity profile in XPPF, given by $U = 1 - y^2$, and in XPCF, given by U = y, is not affected by rotation.

2.2. Linear stability analysis

We use standard linear stability methodology and linearise the governing equation (2.1). Introducing wall-normal velocity v(x, t) and wall-normal verticity $\eta(x, t)$ perturbations gives

$$\left[\left(\frac{\partial}{\partial t} + U \frac{\partial}{\partial x} \right) \nabla^2 - U'' \frac{\partial}{\partial x} - \frac{1}{Re} \nabla^4 \right] v + Ro \frac{\partial \eta}{\partial x} = 0, \tag{2.2a}$$

$$\[\left(\frac{\partial}{\partial t} + U \frac{\partial}{\partial x} \right) - \frac{1}{Re} \nabla^2 \] \eta + \left[U' \frac{\partial}{\partial z} - Ro \frac{\partial}{\partial x} \right] v = 0, \tag{2.2b}$$

where $U' = \mathrm{d}U/\mathrm{d}y$ and $U'' = \mathrm{d}^2U/\mathrm{d}y^2$ and boundary conditions $v = \partial v/\partial y = \eta = 0$ at the walls. Assuming wave-like perturbations $v(\boldsymbol{x},t) = \hat{v}(y)\mathrm{e}^{\mathrm{i}(\alpha x + \beta z - \omega t)}$ and $\eta(\boldsymbol{x},t) = \hat{\eta}(y)\mathrm{e}^{\mathrm{i}(\alpha x + \beta z - \omega t)}$ with wavenumber vector $\boldsymbol{k} = (\alpha,\beta)$ leads to the following eigenvalue problem in matrix form:

$$-i\omega \begin{pmatrix} D^2 - k^2 & 0\\ 0 & 1 \end{pmatrix} \begin{pmatrix} \hat{v}\\ \hat{\eta} \end{pmatrix} + \begin{pmatrix} \mathcal{L}_{OS} & \mathcal{L}_R\\ \mathcal{L}_C & \mathcal{L}_{SQ} \end{pmatrix} \begin{pmatrix} \hat{v}\\ \hat{\eta} \end{pmatrix} = \begin{pmatrix} 0\\ 0 \end{pmatrix}, \tag{2.3}$$

where the Orr–Sommerfeld and Squire operators \mathcal{L}_{OS} and \mathcal{L}_{SQ} and operators \mathcal{L}_R and \mathcal{L}_C are given by

$$\mathcal{L}_{OS} = i\alpha U(D^2 - k^2) - i\alpha U'' - \frac{1}{Re}(D^2 - k^2)^2,$$
 (2.4a)

$$\mathcal{L}_R = i\alpha Ro, \tag{2.4b}$$

$$\mathcal{L}_C = i(\beta U' - \alpha Ro), \qquad (2.4c)$$

$$\mathcal{L}_{SQ} = i\alpha U - \frac{1}{Re}(D^2 - k^2), \qquad (2.4d)$$

with $k^2 = \alpha^2 + \beta^2$, D(.) = d(.)/dy and boundary conditions $\hat{v}(y) = D\hat{v}(y) = \hat{\eta}(y) = 0$ at $y = \pm 1$. This eigenvalue problem (2.3) for ω with eigenvalues $\hat{v}(y)$ and $\hat{\eta}(y)$ for XPPF and XPCF is discretised using Chebyshev polynomials and solved with Matlab routines. The imaginary part ω_i of the complex eigenvalue ω gives the non-dimensional growth rate of the perturbations. Convergence has been checked by changing the number of collocation points.

2.3. Direct numerical simulations

We also carry out DNS to investigate the stability of XPPF and XPCF, using a pseudospectral code that solves (2.1) with Fourier expansions and periodic boundary conditions in x and z directions and Chebyshev polynomials in the y direction and noslip conditions at the walls (Chevalier *et al.* 2014). In the DNS of XPPF the flow rate is fixed. The code has been used in many previous studies (e.g. Brethouwer *et al.* 2012; Brethouwer 2017, 2021).

2.4. Validation of the linear stability analysis

The LSA results for XPPF agree with those of Masuda *et al.* (2008), as we show later. To further validate our LSA we have carried out DNS of XPCF and XPPF with small initial perturbations at three Ro and Re slightly above Re_c . We compared the growth rate of the velocity fluctuations with that of the most unstable mode predicted by LSA. The growth rates match, as shown in the Appendix.

3. Results: linear stability analysis

We first discuss the LSA results. Figure 2 shows the neutral stability curves of XPPF and XPCF. The most unstable mode in XPCF is three-dimensional due to system rotation and the same applies to XPPF, except at very low Ro when a two-dimensional TS mode with $\beta = 0$ is most unstable. The neutral stability curve of this TS mode, which converges for $Ro \rightarrow 0$ to the critical Reynolds number $Re_c = 5772.2$ of NPPF, is also shown. According to figure 2 we can distinguish two asymptotic neutral stability regimes for three-dimensional perturbations in XPCF and XPPF: a low-Ro regime with $Re_c \propto 1/Ro$ at $Ro \rightarrow 0$ and a high-Ro regime with Re_c approaching a low constant value at $Ro \rightarrow \infty$. The transition between these two regimes is at $Ro \sim O(1)$. Since Ro expresses

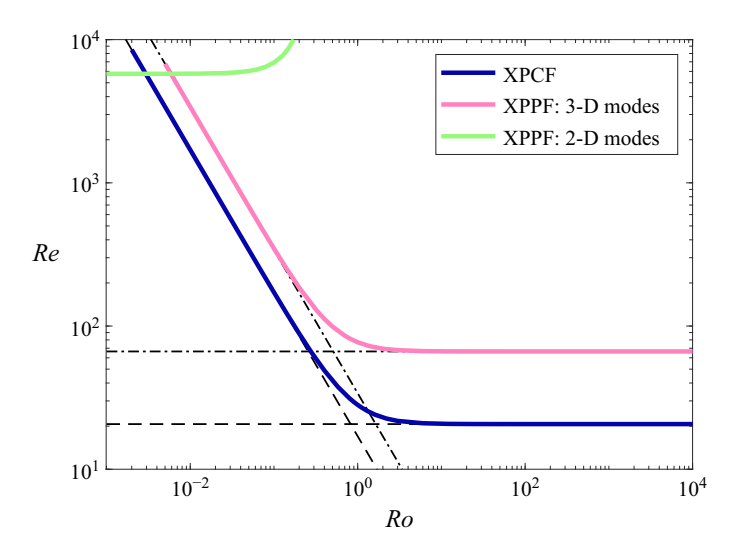


Figure 2. Neutral stability curves of three-dimensional (3-D) modes in XPCF and the two-dimensional (2-D) $\beta = 0$ and three-dimensional modes in XPPF. Horizontal dashed line, $Re = \sqrt{1707.762}/2$; horizontal dashed line, Re = 66.45. Sloped dashed line, Re = 17/Ro; sloped dash-dotted line, Re = 33.923/Ro.

the ratio of system rotation to mean shear rotation, we can call the regime with $Ro \gg 1$ a rotation-dominated regime and the regime with $Ro \ll 1$ a shear-dominated regime.

Masuda *et al.* (2008) already identified these two asymptotic regimes for XPPF. They found $Re_c = 33.923/Ro$ in the low-Ro regime and $Re_c = 66.45$ in the high-Ro regime, shown by dash-dotted lines in figure 2, which match our LSA results. In XPCF, $Re_c \simeq 17/Ro$ when $Ro \to 0$ and $Re_c = 20.6625$ when $Ro \to \infty$, shown by dashed lines in figure 2. The latter Re_c is equal to the minimum critical Reynolds number $Re_c = \sqrt{1707.762}/2 = 20.6625$ in ZPCF occurring at Ro = 1/2, which is explained in the next section. In the high-Ro regime of XPPF something similar happens since Re_c approaches 66.45, which is equal to the minimum Re_c in ZPPF occurring at Ro = 0.3366 (Wall & Nagata 2006).

Figure 3(a,b) shows the wavenumbers of the critical three-dimensional mode α_c and β_c at neutral stability conditions, and figure 3(c) the angle $\theta = \arctan(\alpha_c/\beta_c)$ of the wavenumber vector $\mathbf{k}_c = (\alpha_c, \beta_c)$ with the z axis as a function of Ro in XPPF and XPCF. The critical spanwise wavenumber assumes a constant but different value in the low-Ro and high-Ro regimes, and changes at $Ro \sim O(1)$. In XPPF, $\beta_c = 2.459$ when $Ro \to \infty$, which is the same β_c as in ZPPF at the minimum Re_c at Ro = 0.3366 (Wall & Nagata 2006). Similarly, in XPCF, $\beta_c = 1.558$ when $Ro \to \infty$, which is the same β_c as in ZPCF at the minimum Re_c at Ro = 0.5 (Lezius & Johnston 1976), which in turn is the same critical wavenumber as in Rayleigh–Bénard convection (Chandrasekhar 1961). The angle θ_c and α_c assume a maximum value at $Ro \to O(1)$ and decrease as θ_c , $\alpha_c \propto 1/Ro$ as $Ro \to \infty$, and increase as θ_c , $\alpha_c \propto Ro$ at $Ro \to 0$ in XPPF and XPCF. The critical vortical structures have thus the largest inclination angle with respect to the streamwise direction when $Ro \to O(1)$ and system rotation and mean shear rotation are of the same order, and become more aligned with the streamwise direction when $Ro \to \infty$. The observed alignment of the vortices with the x axis for $Ro \to \infty$ conforms to the Taylor–Proudman theorem.

Figure 4 shows isocontours of the growth rate ω_i in the (α, β) plane at neutral stability conditions in XPPF at high to low Ro. Masuda et al. (2008) showed similar plots for XPPF, although only for cases with $Ro \sim O(1)$. The isocontours are symmetric about the $\beta = 0$

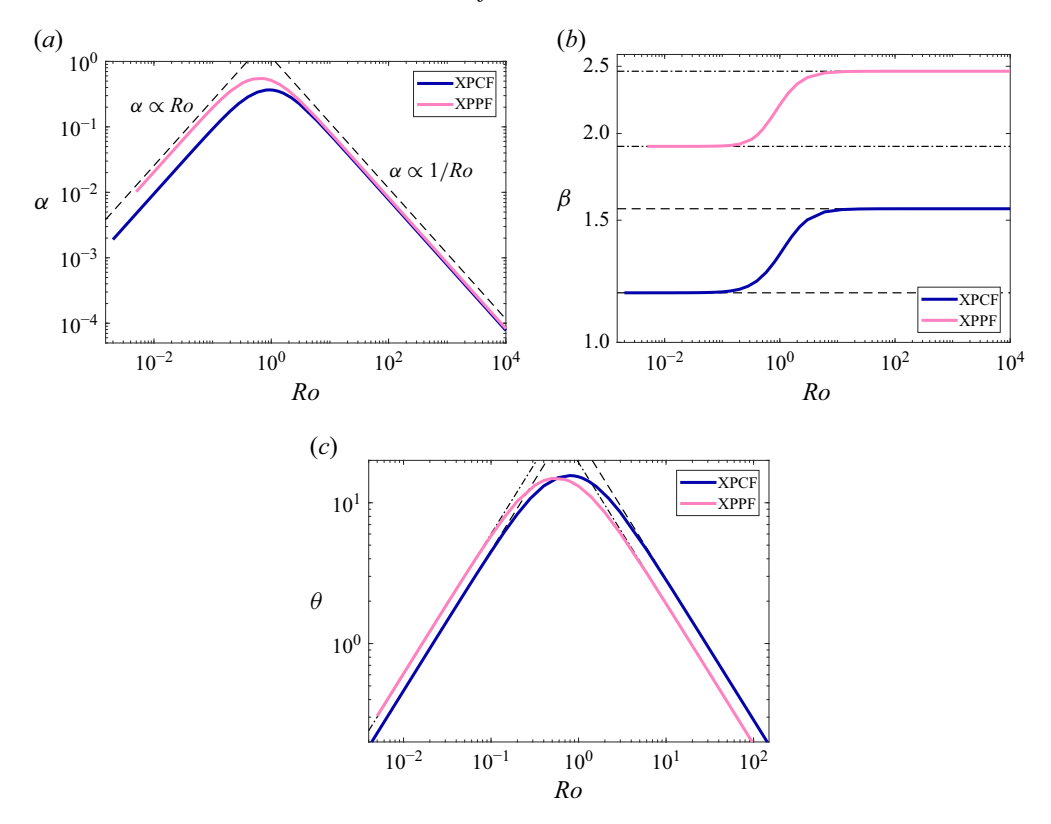


Figure 3. The critical wavenumbers (a) α_c and (b) β_c and (c) angle θ of the wavenumber vector $\mathbf{k}_c = (\alpha_c, \beta_c)$ with the z axis as a function of Ro in XPPF and XPCF. In (b), dashed lines, $\beta = 1.179$ and $\beta = 1.558$; dash-dotted lines, $\beta = 1.917$ and $\beta = 2.459$. In (c), dashed lines, $\theta = 0.5/Ro$ and $\theta = 0.8Ro$; dash-dotted lines, $\theta = 0.3366/Ro$ and $\theta = 1.05Ro$.

axis since the modes with wavenumbers (α, β) and $(\alpha, -\beta)$ have the same growth rate ω_i . This symmetry can be understood by considering the effective rotation rate $\Omega^{ef} = \Omega \hat{x} - (\partial U/2\partial y)\hat{z}$, where the last term is the rotation rate caused by mean shear and \hat{z} is the unit vector in the z direction. In the bottom and top half of the channel, Ω^{ef} has a negative and positive inclination angle with the x axis, respectively, which leads to the same instability on both sides of the channel, but with opposite inclination angles to the x axis. To illustrate this, figure 6(a) visualises the vortical structure of the critical modes in XPPF at Re = 77.02 and Ro = 1. In the bottom and top half of the channel the vortical structures have a negative and positive inclination angle to the x axis caused by modes with $\beta_c > 0$ and $\beta_c < 0$, respectively. Modes with $\beta_c > 0$ and $\beta_c < 0$ also have a larger velocity disturbance and Reynolds shear stresses in the bottom and top half of the channel, respectively (see figure 6c,e). The velocity disturbances and Reynolds shear stresses are obtained by averaging over xz planes. Due to streamwise rotation, all three Reynolds shear stress components become non-zero (Oberlack et al. 2006).

Observations at other Ro are qualitatively similar, although the inclination angle of the vortical structures with the x axis is smaller at lower and higher Ro. When $Ro \rightarrow 0$, two-dimensional modes with $\beta = 0$ become more prominent and are the most unstable modes if Ro is sufficiently small (figure 4d).

In contrast, the isocontours of the growth rate ω_i in the (α, β) plane at neutral stability conditions in XPCF at four Ro, shown in figure 5, are not symmetric about the $\beta = 0$ axis,

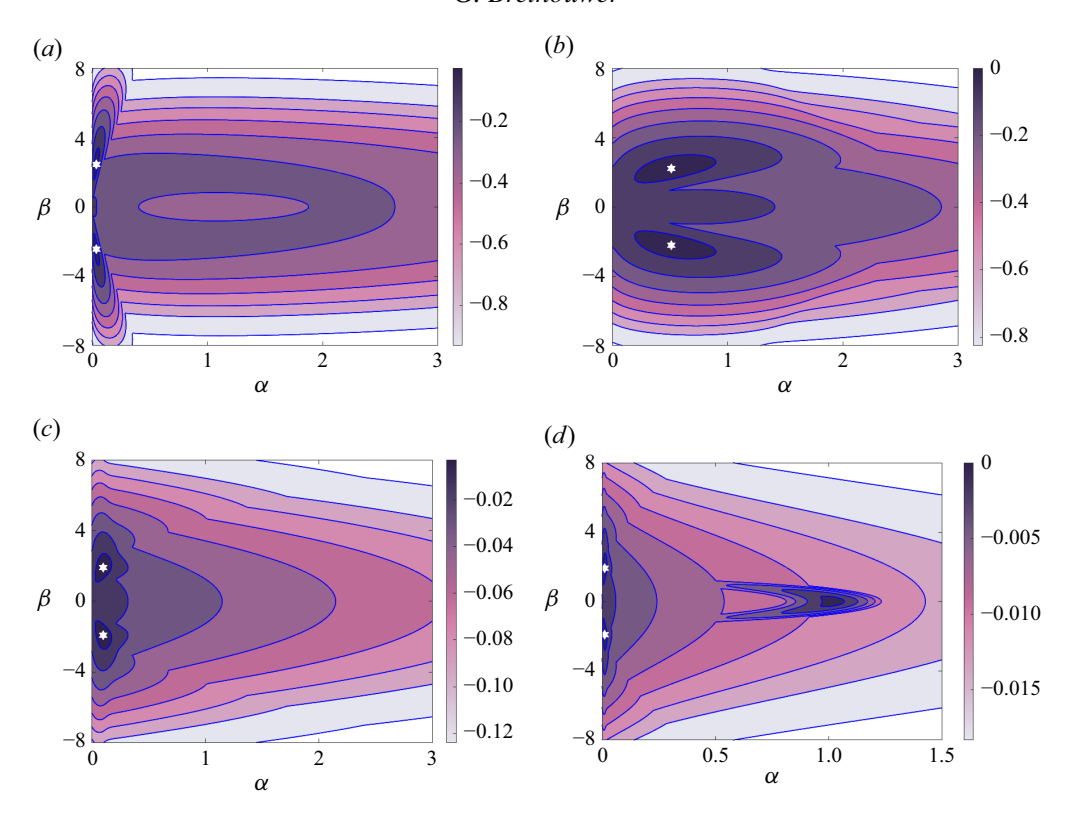


Figure 4. Growth rate ω_i as a function of (α, β) at neutral stability in XPPF: (a) Re = 66.47 and Ro = 24; (b) Re = 77.03 and Ro = 1; (c) Re = 682.8 and Ro = 0.05; (d) Re = 5776 and Ro = 0.000587. The neutrally stable modes are indicated by white stars.

with ω_i generally being greater for $\beta > 0$. Vortical structures of the critical mode with $\beta_c > 0$ in XPCF at Re = 28.14 and Ro = 1, visualised in figure 6(b), are centred in the middle of the channel and have a negative inclination angle with the x axis, like the effective rotation rate Ω^{ef} . Figure 6(d,f) shows that this mode also has the largest streamwise and wall-normal velocity disturbance and Reynolds shear stress amplitudes in the centre of the channel. Observations at other Ro are again quantitatively similar, with the differences that at lower and higher Ro the inclination angle is smaller, and the wall-normal and spanwise velocity disturbances are negligible compared with the streamwise one if $Ro \ll 1$ (not shown here).

4. High-rotation-number asymptotics

We analyse the asymptotic behaviour seen in figures 2 and 3. For classical Rayleigh–Bénard convection between two horizontal flat plates and assuming wall-normal velocity perturbations $v(x, t) = \hat{v}(y)e^{i(\alpha x + \beta z - \omega t)}$ the linearised perturbation equation for a neutral stability mode with $\omega = 0$ can be written as

$$(D^2 - k^2)^3 \hat{v} = -Ra \, k^2 \hat{v}, \tag{4.1}$$

where Ra is the Rayleigh number (Chandrasekhar 1961). The marginally stable mode is stationary with $\omega = 0$. When the problem is non-dimensionalised with the gap width 2δ

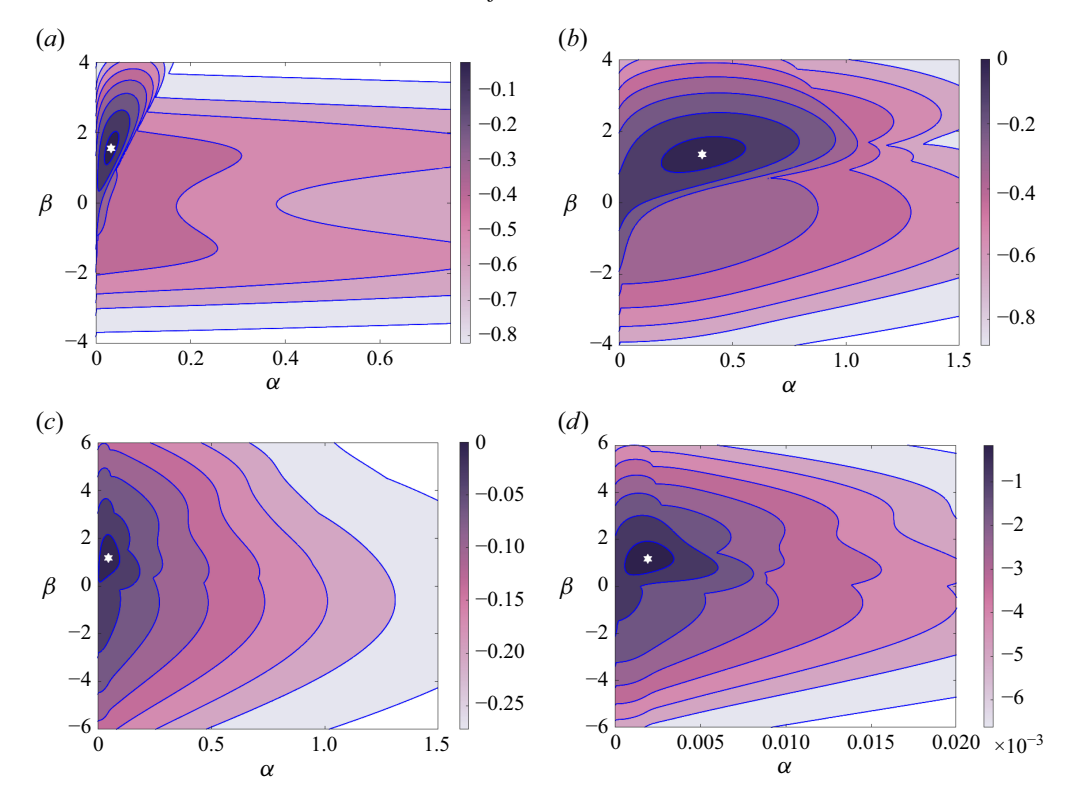


Figure 5. Growth rate ω_i as a function of (α, β) at neutral stability in XPCF: (a) Re = 20.68 and Ro = 24; (b) Re = 28.14 and Ro = 1; (c) Re = 340.9 and Ro = 0.05; (d) Re = 8496 and Ro = 0.002. The neutrally stable mode is indicated by a white star.

as length scale, it can be shown that the critical Rayleigh number $Ra_c = 1707.762$ and wavenumber $k_c = 3.117$ (Chandrasekhar 1961).

We now consider ZPPF and ZPCF. In these cases, the eigenvalue problem of the LSA is the same as for XPPF and XPCF given by (2.3), except that the rotation term αRo is replaced by βRo since the system rotation is about the z direction, that is, $\mathcal{L}_R = \mathrm{i}\beta Ro$ and $\mathcal{L}_C = \mathrm{i}\beta (U' - Ro)$. Since the most unstable mode is two-dimensional with $\alpha = 0$ in ZPPF and ZPCF (Lezius & Johnston 1976; Wall & Nagata 2006), and the neutral stability mode is stationary with $\omega = 0$, we can derive, from the eigenvalue problem (2.3) after substituting \mathcal{L}_R and \mathcal{L}_C , that

$$(D^2 - k^2)^3 \hat{v} = -Re_d^2 Ro(U' - Ro) \beta^2 \hat{v}, \tag{4.2}$$

by eliminating $\hat{\eta}$ from the eigenvalue problem. The boundary conditions for \hat{v} are the same as in Rayleigh–Bénard convection. The perturbation equation for PCF is non-dimensionalised using the gap width 2δ and the velocity difference between the walls $2U_w$, to retain the similarity with the Rayleigh–Bénard convection stability problem, so that $Re_d=4U_w\delta/v=4Re$. For PPF, we keep $Re_d=Re$. Further, U'=1 for PCF. The similarity between perturbation (4.1) for Rayleigh–Bénard convection and (4.2) for ZPCF then leads to $16Re_c^2Ro(1-Ro)=Ra_c$ and $\beta_c=3.117/2=1.558$ if δ is used as length scale (Lezius & Johnston 1976). Consequently, the minimum $Re_c=\sqrt{Ra_c}/2=20.6625$ in ZPCF occurs at Ro=1/2. In this case, Re_c and Re_E coincide, as shown by Joseph & Munson (1970) and Busse (1970), similar to Rayleigh–Bénard flow.

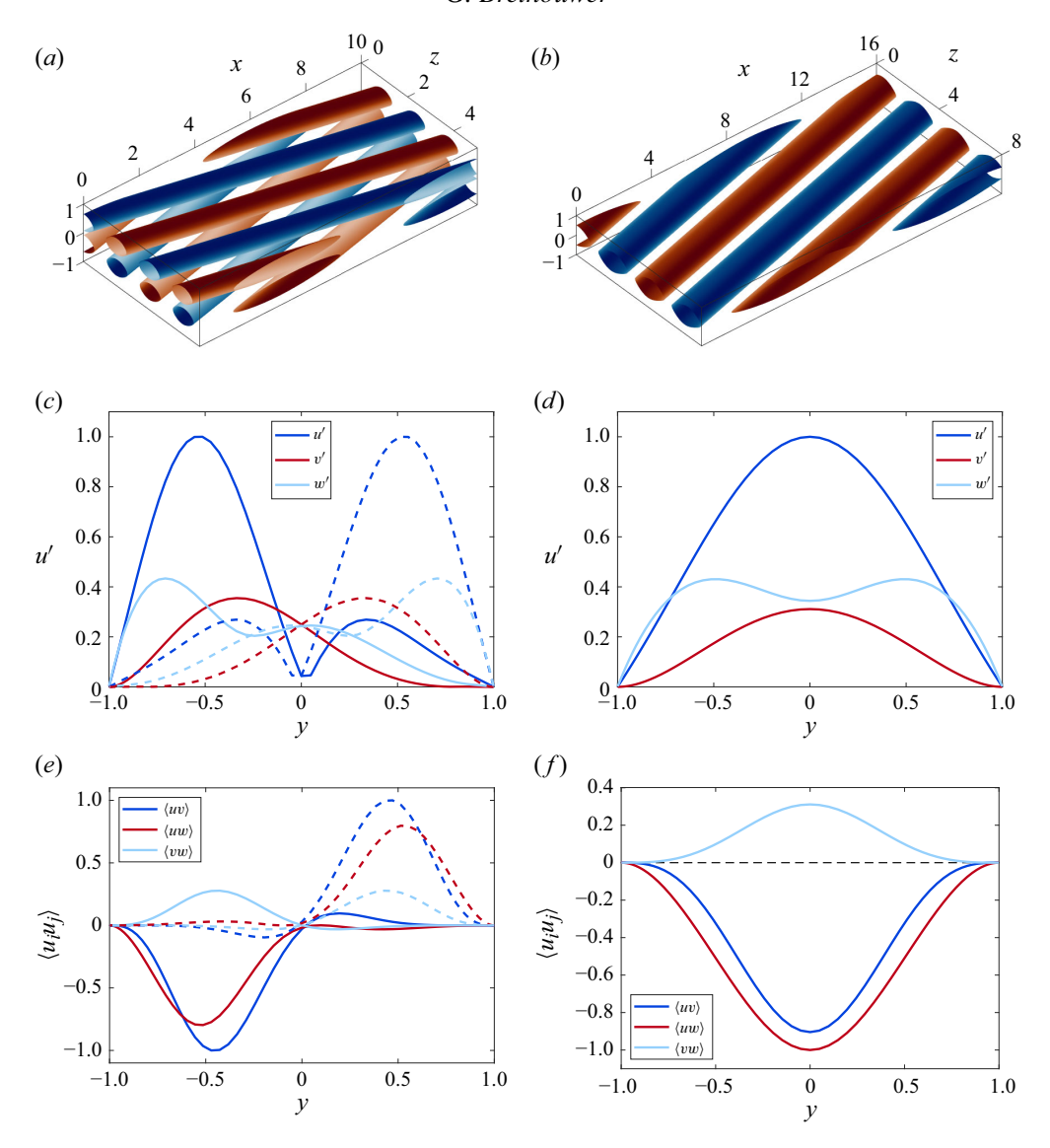


Figure 6. (a) Visualisation using the Q criterion (Hunt, Wray & Moin 1988) and (c) root mean square of the velocity disturbances and (e) the Reynolds shear stresses of the two critical modes with $\beta_c > 0$ and $\beta_c < 0$ shown by the solid and dashed lines, respectively, in XPPF at Re = 77.02 and Ro = 1. (b) Visualisation using the Q criterion (Hunt et al. 1988) and (d) root mean square of the velocity disturbances and (f) the Reynolds shear stresses of the critical mode in XPCF at Re = 28.14 and Ro = 1. The vortices in (a,b) are coloured by the streamwise vorticity with blue and red denoting positive and negative values, respectively.

We return to XPPF and XPCF and apply the same procedure. In XPPF the neutrally stable modes are not stationary; therefore, only $\omega_i = 0$ and $\omega = \omega_r$ with ω_r the (real) wave frequency. Considering neutrally stable modes with $\omega = \omega_r$ and eliminating $\hat{\eta}$ from the eigenvalue problem (2.3), we find that

$$(D^{2} - k^{2})^{3} \hat{v} = -Re_{d}^{2} \alpha Ro \left(\beta U' - \alpha Ro\right) \hat{v} + Re_{d}^{2} \alpha^{2} \mathcal{U}_{X} \mathcal{L}_{X} \hat{v}$$
$$+ iRe_{d} \alpha \left[\mathcal{U}_{X} \left(D^{2} - k^{2}\right)^{2} + \left(D^{2} - k^{2}\right) \mathcal{L}_{X}\right] \hat{v}, \tag{4.3}$$

where $U_X = U - \omega_r/\alpha$ and $\mathcal{L}_X = \mathcal{U}_X(D^2 - k^2) - U''$. Note that the most unstable modes are three-dimensional. In XPCF, U'' = 0 and $U_X = U$ since the neutrally stable modes are stationary ($\omega_r = 0$) if the walls move with the same speed but in opposite directions.

Of the three terms on the right-hand side of (4.3) only the first contains Ro and Ro^2 and therefore dominates if $Ro \gg 1$. This has been verified by comparing the terms using the eigenvalue solver for the LSA. In that case, when $Ro \gg 1$ and only the first term is relevant, (4.2) and (4.3) are equivalent if αRo in (4.3) for XPPF/XPCF is equal to βRo in (4.2) for ZPPF/ZPCF. That is, the perturbation equations are similar when the component of k parallel to the rotation axis, multiplied by the rotation rate, is the same in the streamwise- and spanwise-rotating cases. This implies that the Coriolis force acting on a slightly oblique mode in a rapidly streamwise-rotating flow can have the same effect on the wall-normal velocity perturbation as the Coriolis force acting on a purely streamwise (longitudinal) mode in a spanwise-rotating flow. We know that the minimum critical Re_c in ZPPF and ZPCF occurs at $Ro_{ZPPF}^c = 0.3366$ and $Ro_{ZPCF}^c = 0.5$, respectively (Lezius & Johnston 1976; Wall & Nagata 2006). The similarity of the perturbation equations when αRo in XPPF/XPCF is equal to βRo in ZPPF/ZPCF means that β_c and Re_c in the streamwise-rotating cases are the same as β_c and minimum Re_c in the spanwise-rotating cases. Furthermore, Re_c in XPPF and XPCF is found for that θ when $Ro \tan \theta = Ro_{ZPPF}^c = 0.3366$ and $Ro \tan \theta = Ro_{ZPCF}^c = 0.5$, respectively, where $\theta =$ $\arctan(\alpha/\beta)$ is again the angle of **k** with the z axis in the streamwise-rotating case. We can approximate $\tan \theta \simeq \theta$ when $Ro \gg 1$, so that the critical mode in XPPF and XPCF obeys $\theta = 0.3366/Ro$ and $\theta = 0.5/Ro$, respectively. With $Ro \tan \theta = Ro_{ZPCF}^c = 0.5$, (4.3) for XPCF becomes

$$(D^2 - k^2)^3 \hat{v} = -\frac{1}{4} R e_d^2 \beta^2 \hat{v}. \tag{4.4}$$

The similarity between (4.4) and (4.1) for Rayleigh–Bénard convection gives $\beta_c = 1.558$ and $Re_d^2/4 = 4Re^2 = Ra$; therefore, $Re_c = \sqrt{Ra_c}/2 = 20.6625$ in XPCF when $Ro \to \infty$. The results of these considerations, $Re_c = 20.6625$, $\beta_c = 1.558$ and $\theta_c = 0.5/Ro$ in XPCF and $Re_c = 66.45$, $\beta_c = 2.459$ and $\theta_c = 0.3366/Ro$ in XPPF, are shown by dashed lines in figures 2 and 3(b,c), confirming that these values are approached for $Ro \gg 1$.

In summary, the critical Reynolds number Re_c and wavenumber β_c in XPPF and XPCF become independent of Ro and approach the minimum Re_c and corresponding β_c in ZPPF and ZPCF, respectively, for $Ro \rightarrow \infty$. Moreover, the linear stability of ZPCF as well as XPCF at $Ro \rightarrow \infty$ share similarities with that of Rayleigh–Bénard convection. For $Ro \lesssim 5$ in the streamwise-rotating cases, the remaining terms on the right-hand side of (4.3) become significant, and the similarity with the spanwise rotating cases is lost.

In XPCF, the critical Reynolds number for energy instability Re_E is identical to that in NPCF because energy stability is unaffected by rotation (Joseph & Munson 1970; Joseph 1976); the Coriolis term vanishes in the energy equation. In this case, the eigenvalue problem for energy instability is also equivalent to that of the LSA for Rayleigh–Bénard convection given by (4.1) (Joseph 1966), yielding $Re_E = \sqrt{Ra_c}/2 = 20.66$ for both NPCF and XPCF (Busse 1970; Joseph & Munson 1970; Reddy & Henningson 1993; Barletta & Mulone 2024). The present analysis shows that Re_c converges to this same value in the limit $Ro \to \infty$, showing that linear and energy stability coincide, ruling out subcritical transition. Busse (1970) demonstrated the same result for ZPCF at Ro = 0.5 and noted its extension to XPCF as $Ro \to \infty$. Joseph & Munson (1970) and Joseph (1976), using a different approach within the framework of spiral flow between concentric cylinders, confirmed the coincidence of energy and linear stability in XPCF at $Ro \to \infty$ for $\alpha \to 0$, $\theta Ro = 0.5$ and $\beta = 1.558$, consistent with the present results. This mode is the most

susceptible to transient growth in NPCF due to the non-normality of the linearised Navier–Stokes operator (Reddy & Henningson 1993).

Thus, streamwise rotation, like spanwise anti-cyclonic rotation, preferentially destabilises the mode showing maximal transient growth without rotation, explaining the strong destabilising effect of rotation and making the linearised Navier–Stokes operator effectively normal again. A similar argument applies to the XPPF case; further details can be found in the study by Jose & Govindarajan (2020).

In the asymptotic limit $Ro \to 0$ of XPPF and XPCF the critical vortices also align with the x axis and thus k_c aligns with the z axis, giving $\alpha = \beta \tan \theta \simeq \beta \theta$. The first term on the right-hand side of (4.3) then approaches $-Re_d^2\theta RoU' \beta^2\hat{v}$ since $\alpha Ro \ll \beta U'$. When $\theta \propto Ro$, $Re_d \propto 1/Ro$ and β is constant, all three terms on the right-hand side of perturbation (4.3) remain constant and significant. This behaviour, $\theta_c \propto Ro$ and $Re_c \propto 1/Ro$ (noting that $Re_c \propto Re_d$) is observed in figures 2 and 3(c) in XPPF and XPCF in the limit $Ro \to 0$.

5. Results: direct numerical simulations

Subcritical transition to turbulence can occur in NPPF and NPCF, resulting in stable coexisting laminar and turbulent states (Grossmann 2000; Manneville 2015). However, when Re is gradually reduced, uniformly turbulent NPPF and NPCF become transitional before relaminarising, and turbulent–laminar flow patterns develop if the flow domain is sufficiently large (Shimizu & Manneville 2019; Tuckerman et al. 2020). Subcritical transition and transitional regimes have also been observed in ZPCF, at higher Re than in NPCF, when the rotation is cyclonic and $Re_c \rightarrow \infty$ (Tsukahara et al. 2010; Brethouwer et al. 2012), but not yet when the rotation is anti-cyclonic and destabilises the flow (Alfredsson & Persson 1989; Tsukahara et al. 2010). Instead, regular and steady streamwise vortices are observed at Re near Re_c . In ZPPF subcritical transition has only been observed at very low Ro (Jose et al. 2017), and turbulent–laminar patterns only appear in some Re-Ro range on the channel side stabilised by rotation (Brethouwer 2017, 2019).

It is not yet known whether a subcritical transition can occur, and whether the transitional regime exists in XPPF and XPCF. We carry out DNS of XPPF and XPCF to address these questions. The DNS cover the range $Re \le 2000$ in XPPF and $Re \le 1000$ in XPCF, and $0 \le Ro \le 0.8$, and also include non-rotating and rapidly rotating cases at Ro = 24. A computational domain $L_x/\delta \times L_z/\delta$ of 110×50 and 250×125 is used in the DNS of XPPF and XPCF, respectively, and a spatial resolution of $512 \times 33 \times 512$ in the streamwise, wall-normal and spanwise directions, unless otherwise specified. These computational domain sizes are similar to those used in DNS by Brethouwer *et al.* (2012) and large enough to accommodate large-scale turbulent-laminar patterns. The resolution in the XPCF cases is finer than that determined by Manneville & Rolland (2011) for relatively well-resolved uniformly turbulent and transitional regimes in NPCF. The formation of turbulent-laminar patterns in NPCF is not very sensitive to resolution, with only a gradual downward shift of the Re threshold for patterns when resolution becomes coarse (Manneville & Rolland 2011).

To determine the lower Re threshold of sustained vortices or turbulence at a given Ro, we initialise the DNS with turbulent flow at sufficiently high Re and reduce Re in small steps until the flow becomes laminar. The lower threshold for sustained turbulence, called Re_t , is defined as the lowest Re at which turbulence or turbulent patterns persist for a time period of at least $2 \times 10^5 (\delta/U_{cl,w})$ in our DNS. This does not preclude that turbulence or turbulent patterns eventually disappear on longer time scales.

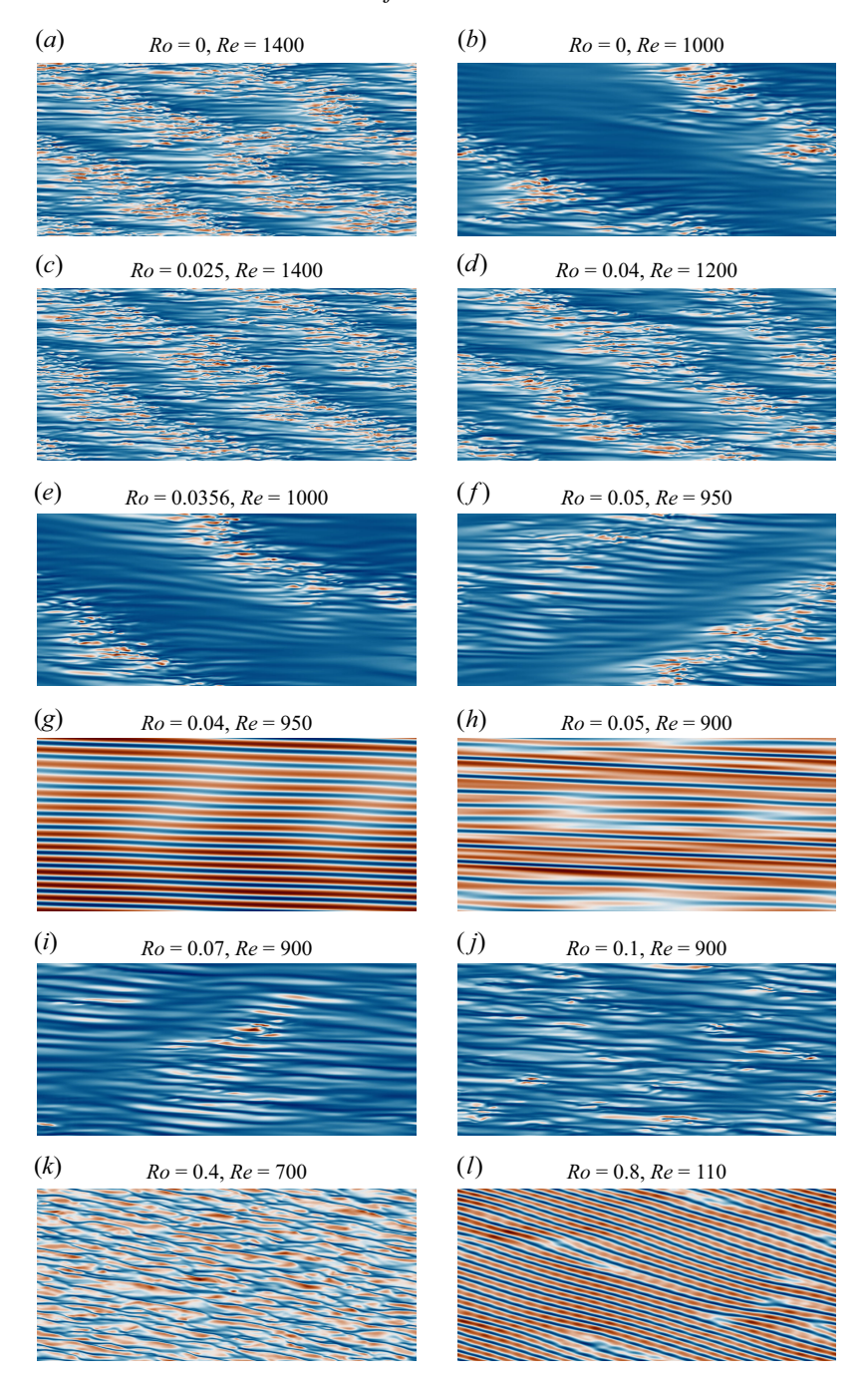


Figure 7. Visualisation of the streamwise velocity field in XPPF in an xz plane at y = -0.9.

Firstly, we discuss DNS results of PPF using visualisations of the instantaneous streamwise velocity field in an xz plane near the wall at y = -0.9 shown in figure 7. Additional visualisations of the velocity field are presented in the supplementary material available at https://doi.org/10.1017/jfm.2025.10723. Hereafter, $Re = U_{cl}\delta/\nu$ for PPF, where U_{cl} is the centreline velocity of the laminar base flow. The bulk Reynolds number

 $Re_b = U_b \delta/v = 2Re/3$, where U_b is the bulk mean velocity. We observe in NPPF (Ro = 0) uniform turbulence at Re = 2000, and transitional turbulence with oblique turbulent–laminar patterns at Re = 1400 (figure 7a). When Re decreases, the turbulent patterns become less structured and at $Re_t = 1000$ one oblique turbulent band persists in a laminar-like flow environment (figure 7b), while below Re_t the flow relaminarises.

These results for NPPF are broadly consistent with those of Shimizu & Manneville (2019). They observed local relaminarisation at $Re \approx 1800$ and turbulent patterns at lower Re until about 800 in NPPF. This Re threshold for turbulent patterns is lower than in our DNS, which may be a result of the larger computational domain in their study, different simulation time period and other flow forcing (constant pressure gradient in their study versus constant mass flow in our study). However, using a larger computational domain in our DNS is prohibitively expensive when covering a wide range of Ro, which requires many simulations.

In XPPF we also observe at low $Ro \lesssim 0.05$ a transitional regime with sustained turbulent–laminar patterns (figure 7c,d), sometimes forming oblique bands, at low Re until $Re_t = 1000$ at $Ro \leqslant 0.04$ and $Re_t = 950$ at Ro = 0.05 (figure 7e,f). The observed patterns span the whole channel gap width, as in NPPF, but in the present configuration we observe differences in the DNS at low Ro. At Ro = 0, 0.025 and 0.0356 the flow relaminarises if $Re < Re_t$, while at Ro = 0.04 and 0.05 the turbulent patterns disappear if $Re < Re_t$, but the flow does not relaminarise since $Re_t > Re_c$. Instead, we observe regular vortices nearly aligned with the streamwise direction without signs of turbulence (figure 7g,h). When Re is further reduced the flow only relaminarises once $Re \leqslant Re_c$. At Ro = 0.07 we observe spotty turbulent structures at low Re until $Re \approx 900$ (figure 7i), and more regular vortices at lower Re until Re_c when the flow relaminarises. When Ro increases, the spotty structures gradually disappear and turbulence becomes more uniform (figure 7i,k). The flow becomes less turbulent when Re approaches Re_c (figure 7i) and fully relaminarises when $Re < Re_c$.

We now study XPCF using visualisations of the instantaneous streamwise velocity field in an xz plane at the centre at y=0 shown in figure 8. Additional visualisations of the velocity field are again presented in the supplementary material. The behaviour of XPCF is qualitatively similar to that of XPPF. In DNS of NPCF (Ro=0) we observe uniform turbulence at Re>400, local relaminarisation at $Re\simeq400$ and turbulent–laminar patterns at lower Re, which are sustained until $Re_t=340$ (figure 8a). The patterns form clearer structured oblique bands than in NPPF. These observations are consistent with previous studies (Prigent et~al.~2003; Duguet et~al.~2010), although in DNS by Duguet et~al.~2010) turbulent–laminar patterns could also be sustained at somewhat lower $Re\simeq324$. This may be caused by a difference in the computational domain size and simulation time period, which was $2\times10^4(\delta/U_w)$ in the DNS by Duguet et~al.~(2010). In our DNS, turbulent patterns persist for such a time period at Re=330, but after a time period of nearly $10^5(\delta/U_w)$ the flow relaminarises.

Observations in DNS of XPCF at Ro = 0.025, 0.05, 0.07 and 0.1 are similar. We observe uniform turbulence at Re > 400, local flow relaminarisation at $Re \simeq 400$ and turbulent patterns and oblique bands develop when Re is gradually reduced (figure 8b,c,e). Full relaminarisation of the flow happens when Re < 340 at Ro = 0.025 and Re < 330 at Ro = 0.05. The oblique bands span the whole channel gap width, as in NPCF and ZPCF at low cyclonic rotation rates (Brethouwer $et\ al.\ 2012$). At Ro = 0.07 and 0.1 the turbulent pattern disappears when Re < 310 and Re < 300, respectively, but the flow does not relaminarise when Re is reduced as long as $Re > Re_c$, since regular vortices persist with localised disturbances but without larger turbulent patterns (figure 8d,f). The flow relaminarises once $Re < Re_c$.

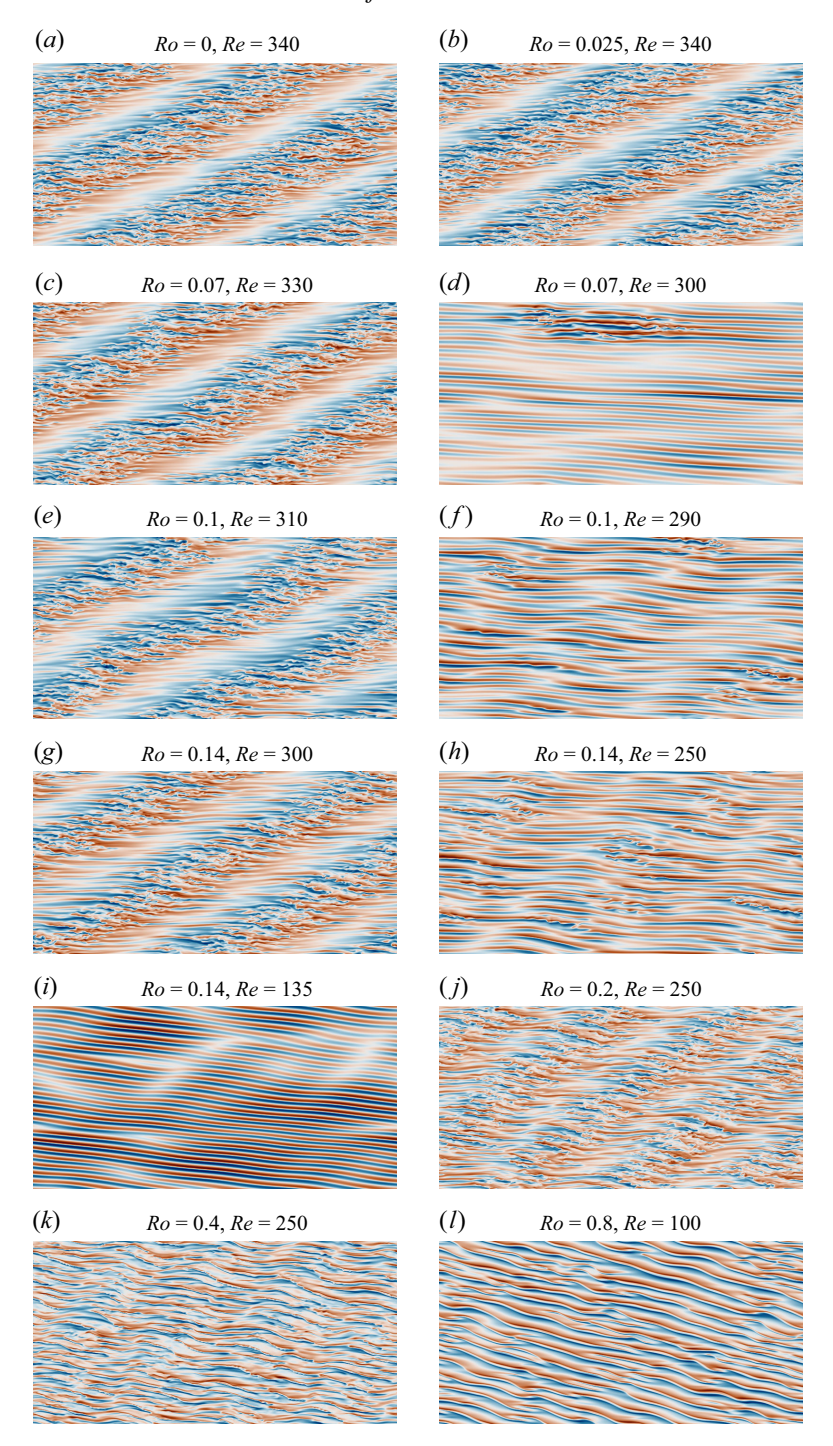


Figure 8. Visualisation of the streamwise velocity field in XPCF in an xz plane at y = 0.

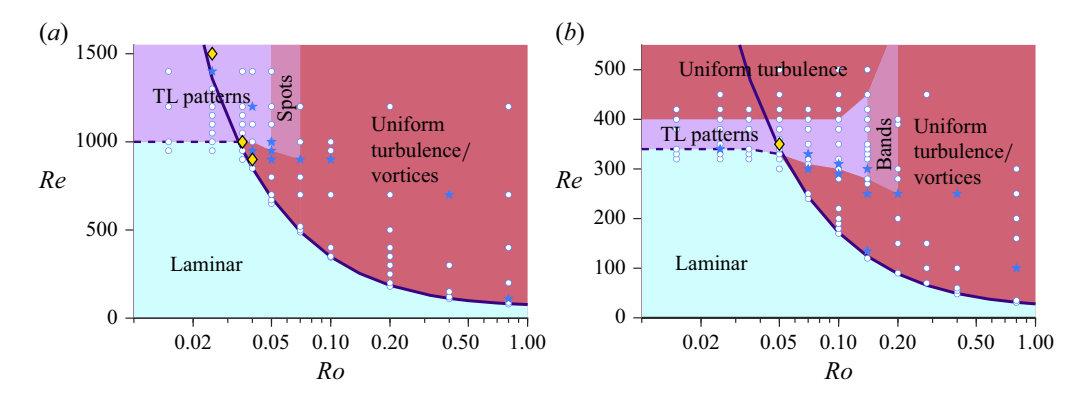


Figure 9. Flow regimes as a function of Ro and Re in (a) XPPF and (b) XPCF. Four flow regimes are distinguished (each marked by a different colour): a regime with (i) uniform/featureless turbulence or vortices, (ii) laminar flow, (iii) turbulent–laminar (TL) patterns and (iv) spotty structures or spots (XPPF)/band-like structures (XPCF) but no clear turbulent and laminar flow regions. Also shown are the neutral stability curve (solid line), subcritical threshold Re_t (dashed line), conditions at which two stable non-laminar flow states coexist (yellow diamonds), conditions at which DNS were performed (white circles) and conditions corresponding to the visualisations shown in figures 7 and 8 (blue stars).

Oblique band-like structures appear in XPCF at Ro = 0.14 if $Re \lesssim 450$. These bands become more distinct when Re is further lowered (figure 8g), but between the turbulent bands we see streamwise vortices and not the clear laminar-like flow regions, as at lower Ro. The turbulent bands disappear when Re < 280. Localised disturbances and vortical motions persist at Re near Re_t (figure 8h), while only streamwise vortices persist at lower Re (figure 8i) until $Re < Re_c$ and the flow relaminarises. At Ro = 0.2 we observe oblique patterns if $250 \lesssim Re \lesssim 600$ with different turbulence activity but without laminar-like flow regions (figure 8j). With increasing Ro the oblique patterns gradually disappear (figure 8k) and we only see uniform turbulence or regular vortices when $Re > Re_c$ (figure 8l).

Figure 9 shows a survey of the observed flow regimes as a function of Re and Ro in the DNS of XPPF and XPCF. We distinguish between four flow regimes: a fully laminar regime; a transitional regime with local relaminarisation or large-scale turbulent–laminar patterns; a regime with a less clear distinction between turbulent and laminar flow regions but with large-scale patterns; and a regime with uniform turbulence or vortical motions. In XPPF and XPCF, organised and steady vortices appear at higher Ro near Re_c . As Re increases further, these vortices gradually become more unsteady and chaotic, ultimately transitioning into a uniformly turbulent flow. As a result, it was not possible to define a sharp transition between the regimes characterised by uniform vortices and uniform turbulence; therefore, these regimes are not treated separately.

Furthermore, we have not observed the variety of vortical structures reported previously for ZPCF (Tsukahara *et al.* 2010; Suryadi, Segalini & Alfredsson 2014) and Taylor–Couette flow (Andereck, Liu & Swinney 1986). Also, no clear qualitative differences were evident in the uniform turbulence regime of XPCF for $Ro \leq 0.14$ and only at higher rotation rates (e.g. Ro = 0.8) do the effects of rotation on the vortical structures become noticeable (not shown here). Developing a more detailed and refined regime map would require extensive additional simulations and analysis and is therefore beyond the scope of the present study.

At some Ro we observe two coexisting stable regimes in XPPF and XPCF at a fixed Re somewhat higher than Re_c : a regime with regular vortices nearly aligned with the streamwise direction but without turbulent motions, and a regime with transitional or turbulent flow. This regime with regular vortices appears when the DNS is initialised with

a laminar flow with small noise. These two coexisting non-laminar flow regimes are only observed in a narrow *Ro* range (see figure 9). This differs from NPPF and NPCF and XPPF and XPCF at low *Ro* when under subcritical conditions only transitional and laminar flow regimes are stable.

Figure 9 shows that subcritical transition can be triggered at low Ro in XPPF and XPCF since $Re_t < Re_c$, while the flow relaminarises if $Re < Re_t$. At higher Ro, when $Re_t > Re_c$ or when the transitional regime is absent, we cannot find evidence of subcritical transition since in all our DNS, XPPF and XPCF then relaminarise if $Re < Re_c$. This absence of subcritical transition in XPPF and XPCF at higher Ro was checked by initialising the DNS in two different ways: (i) with a uniformly or transitional turbulent flow at higher Re and subsequently reducing Re in steps until Re was slightly below Re_c and (ii) with a flow with strong disturbances at Re slightly below Re_c . In both cases, the flow relaminarised in the DNS. The crossover from the low-Ro range with subcritical transition to high-Ro range without subcritical transition is at $Ro \simeq 0.034$ in XPPF and $Ro \simeq 0.05$ in XPCF. Observations do not change fundamentally for Ro > 1, that is, turbulent motions or vortices only develop if $Re > Re_c$. In ZPPF and ZPCF, there is likewise no evidence of subcritical transition once rotation has substantially reduced Re_c (Alfredsson & Persson 1989; Tsukahara et al. 2010). Moreover, in XPCF, subcritical transition must vanish entirely in the limit $Ro \to \infty$, since in this limit Re_c and Re_E coincide, implying that transient growth cannot occur for $Re < Re_c$. Figure 9 further shows that a transitional regime with turbulent-laminar patterns is observed in XPPF and XPCF, as in NPPF and NPCF, at low Ro but not at higher Ro. These patterns develop even though streamwise rotation acts as destabilising and lowers Re_c , while in ZPCF turbulent-laminar patterns are so far only observed when rotation is cyclonic and stabilises the flow (Tsukahara et al. 2010; Brethouwer et al. 2012). The Re range with turbulent-laminar patterns is fairly constant with Ro. In XPCF we observe a transitional regime at $340 \le Re \le 400$, and in XPPF at $Re \gtrsim 1000$ with the upper bound not determined here. Subcritical transition in XPPF and XPCF is thus only observed when Re_c is higher than the lower bound for turbulent–laminar patterns, that is, when $Re_c \gtrsim 1000$ in XPPF and $Re_c \gtrsim 340$ in XPCF.

Interestingly, we observe a transitional regime with turbulent–laminar patterns in XPPF and XPCF in a small range of Ro when $Re > Re_c$, unlike in NPPF and NPCF where this regime only appears if the flow is subcritical. This suggests that in this small Ro range, patterns can emerge by lowering and raising Re. Indeed, in XPPF at Ro = 0.04 and 0.05 turbulent laminar patterns emerge in our DNS starting not only from a turbulent flow at higher Re and subsequently lowering Re, but also from a flow with vortices but without turbulence at lower Re and subsequently increasing Re.

In fact, we can observe the formation of turbulent–laminar patterns at $Re > Re_c$ in XPPF and XPCF with laminar flow and some noise as initial condition. To show this, we carry out DNS of XPPF at Re = 1200 and 1500 and Ro = 0.04 ($Re_c = 852$) and Ro = 0.05 ($Re_c = 683$) with a computational domain size of $242 \times 2 \times 110$ and resolution of $1536 \times 65 \times 1536$ in the streamwise, wall-normal and spanwise directions, respectively, as well as DNS of XPCF at Re = 350 and Ro = 0.07 ($Re_c = 244$) and Ro = 0.1 ($Re_c = 172$) with a computational domain size of $750 \times 2 \times 375$ and resolution of $1920 \times 49 \times 1920$ in the streamwise, wall-normal and spanwise directions, respectively. These domains and resolutions are larger than in our other DNS of XPPF and XPCF to show the robustness of the observations. The initial condition is a laminar base flow with small noise.

Initially, a linear instability occurs in all six DNS since $Re > Re_c$, leading to an exponential growth of u' and v'. See figures 10(a) and 10(b) for XPPF at Ro = 0.04 and XPCF at Ro = 0.07, respectively. Here, u' and v' are the streamwise and wall-normal velocity fluctuations integrated over the whole volume. After this transient period u' and v'

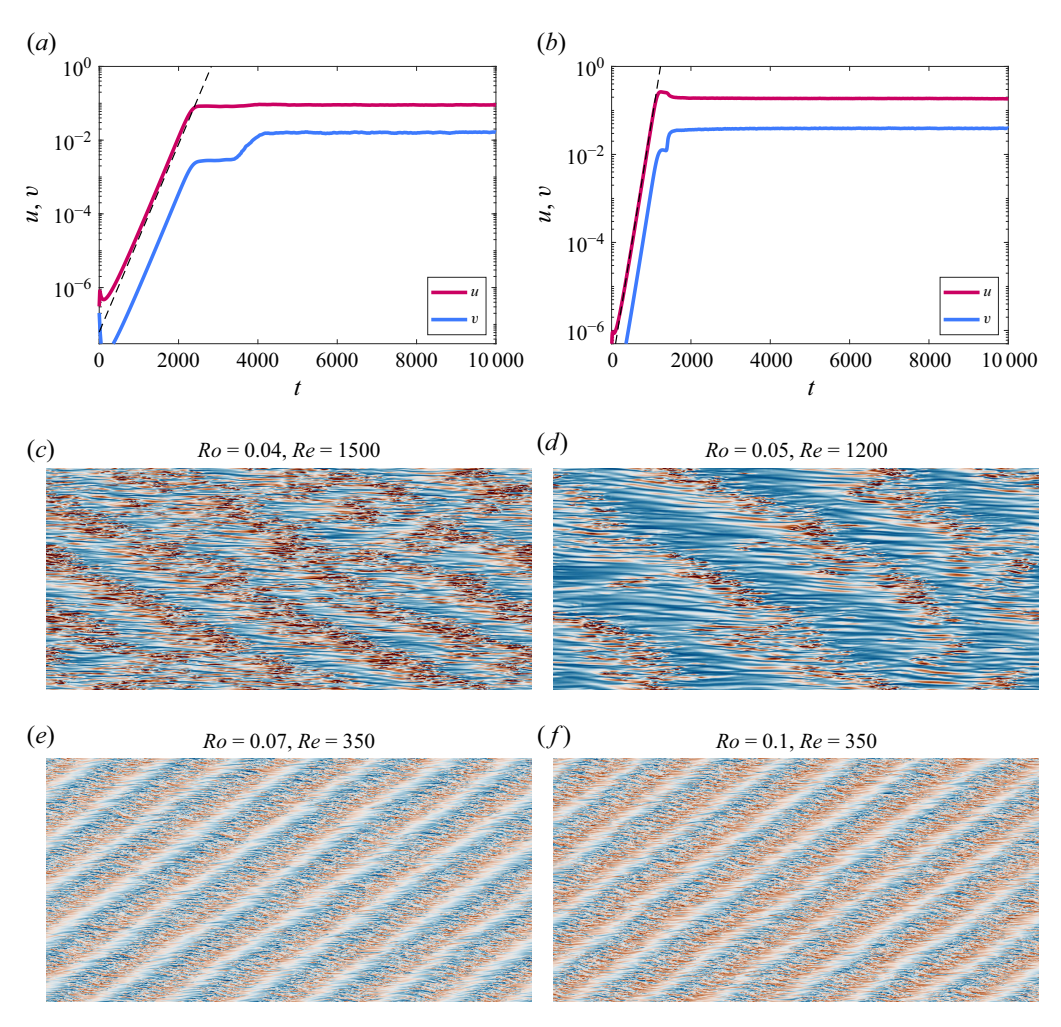


Figure 10. Time series of the streamwise (red line) and wall-normal (pink line) velocity fluctuations in (a) XPPF at Ro = 0.05 and Re = 1200 and (b) XPCF at Ro = 0.1 and Re = 350. Visualisation of the streamwise velocity field in an xz plane (c,d) at y = -0.9 in XPPF and (e,f) at y = 0 in XPCF.

saturate, and turbulent–laminar patterns appear, which develop into sustained oblique turbulent–laminar bands in our DNS of XPPF and XPCF (see figure 10c-f), with similar results for the other two XPPF cases. These results show that in a limited Ro range turbulent–laminar patterns develop under subcritical and supercritical conditions in XPPF and XPCF. By contrast, in DNS at lower Ro with $Re_t < Re < Re_c$, that is, DNS of XPPF at Re = 1500, Ro = 0 ($Re_c = 5772$) and Re = 1200, Ro = 0.025 ($Re_c = 1359$), and DNS of XPCF at Re = 350, Ro = 0 ($Re_c \to \infty$) and Re = 350, Ro = 0.025 ($Re_c = 680$) (not shown here), transition to turbulence and formation of turbulent–laminar patterns only occur when the initial noise levels are finite.

Turbulent–laminar patterns have not yet been observed in ZPCF under supercritical conditions (Tsukahara *et al.* 2010), whereas such patterns can develop in ZPPF, though only on the channel side stabilised by rotation (Brethouwer 2017). It is possible that the dominant streamwise roll cells, triggered by the strongly destabilising effect of anti-cyclonic spanwise rotation, inhibit the formation of turbulent–laminar patterns. In Taylor–Couette flow, turbulent–laminar bands appear as spiral patterns under subcritical

(Meseguer *et al.* 2009*a*; Burin & Czarnocki 2012) and supercritical (Meseguer *et al.* 2009*b*; Wang *et al.* 2022) conditions. We note similarities with the XPPF and XPCF cases considered here, in which turbulent–laminar patterns also appear under subcritical and supercritical conditions.

Berghout *et al.* (2020) and Wang *et al.* (2023) performed DNS of Taylor–Couette flow with counter-rotating cylinders in the supercritical regime, analysing the formation and statistical characteristics of these spiral patterns. Their observed spiral patterns closely resemble those found in subcritical NPCF (Wang *et al.* 2023). However, in Taylor–Couette flow, weak vortices persist near the inner cylinder within the laminar-like regions due to the centrifugal instability of the base flow. A similar phenomenon occurs in XPCF under supercritical conditions exhibiting turbulent–laminar patterns; despite significantly weaker fluctuations, streamwise-oriented vortices remain visible within the laminar-like flow regions (see e.g. figure 8*e*,*g*).

6. Conclusions

We carried out LSA of PPF and PCF subject to streamwise system rotation. Linear stability analysis of streamwise-rotating PPF has already been performed by Masuda *et al.* (2008), but we have extended it and compared it with the PCF case. Three-dimensional perturbations are considered since the most unstable modes are inclined to the streamwise direction, in contrast to spanwise-rotating PPF and PCF in which two-dimensional perturbations with streamwise wavenumber $\alpha = 0$ are most unstable (Lezius & Johnston 1976; Wall & Nagata 2006).

Linear stability analysis of streamwise-rotating PCF shows an asymptotic regime at $Ro \ll 1$ with $Re_c \propto Ro$, and another asymptotic regime at $Ro \gg 1$ with Re_c approaching a constant value, as in streamwise-rotating PPF (Masuda *et al.* 2008). In both asymptotic regimes, the critical spanwise wavenumber β_c approaches a constant value, and the critical vortices become increasingly streamwise-aligned.

The minimum critical Reynolds number $Re_c = 20.66$ of streamwise-rotating PCF at $Ro \to \infty$ is equal to the minimum Re_c of spanwise-rotating PCF at Ro = 0.5 (Lezius & Johnston 1976). Likewise, $Re_c = 66.45$ of streamwise-rotating PPF at $Ro \to \infty$ is equal to the minimum Re_c of spanwise-rotating PPF occurring at Ro = 0.3366 (Wall & Nagata 2006). These results follow from the equation for the wall-normal velocity perturbation. We also show that the linear stability of streamwise-rotating PCF is related to Rayleigh–Bénard convection, like that of spanwise-rotating PCF. In all cases, $\beta_c = 1.558$ and the minimum Re_c in streamwise- and spanwise-rotating PCF at $Ro \to \infty$ and Ro = 0.5, respectively, is related to the critical Raleigh number Ra_c as $Re_c = \sqrt{Ra_c}/2$.

We carried out DNS of streamwise-rotating PPF and PCF in a range of Re and Ro to investigate flow characteristics at low Re and whether a subcritical transition can occur. Our DNS show that a subcritical transition can occur in both flow cases at low Ro but not at higher Ro, since in all simulations the flow then fully relaminarises once $Re < Re_c$. We find that at low Ro the flow can become transitional and sustained large-scale turbulent–laminar patterns can develop at sufficiently low Re. These turbulent–laminar patterns can, especially in streamwise-rotating PCFs, form clear band-like structures. In a small Ro range, turbulent–laminar patterns emerge under supercritical conditions when $Re > Re_c$. We have carried out DNS of streamwise-rotating PPF and PCF to show that under such conditions turbulent–laminar patterns can develop from a growing linear instability when the DNS are initialised by a laminar flow with small noise.

Supplementary material. Supplementary material is available at https://doi.org/10.1017/jfm.2025.10723.

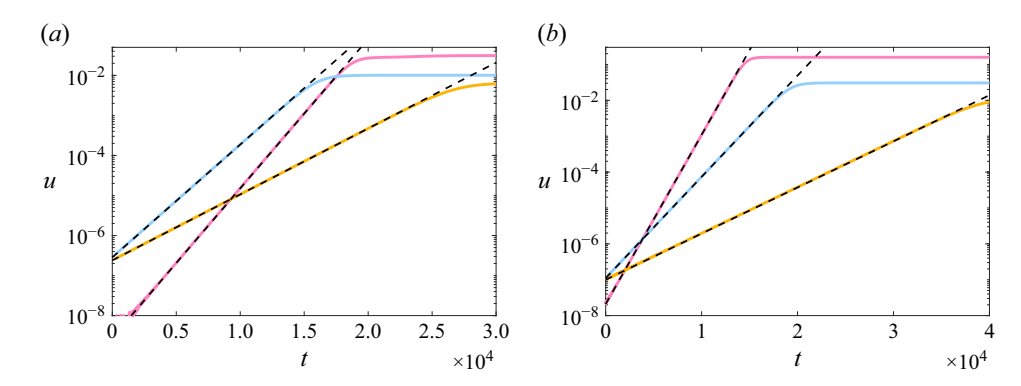


Figure 11. Comparison between the growth of the streamwise velocity fluctuation in DNS of XPPF at (a) Ro = 0.05 and Re = 725 (pink line), Ro = 0.8 and Re = 82.2 (light blue line), Ro = 24 and Re = 66.57 (amber line), and DNS of XPCF at (b) Ro = 0.05 and Re = 370 (pink line), Ro = 0.8 and Re = 31.35 (light blue line), Ro = 24 and Re = 20.7 (amber line), and the growth rate predicted by LSA at the same Ro and Re (dashed lines).

Acknowledgements. NAISS is acknowledged for providing computational resources in Sweden.

Funding. This research received financial support from the Swedish Research Council through grant number 2021-03967.

Declaration of interests. The author reports no conflict of interest.

Appendix. Comparison of LSA and DNS

To validate the LSA we have performed DNS of XPCF and XPPF with small initial perturbations at Ro = 0.05, 0.8 and 24 and Re slightly above Re_c . Figure 11 shows the growth of the root mean square of the velocity fluctuations in the DNS of XPPF and XPCF as well as the growth rate of the most unstable mode predicted by LSA at the same Ro and Re as in the DNS. The computational domain size in all DNS is taken as $L_x = 4\pi/\alpha$ and $L_z = 8\pi/\beta$, where α and β are the streamwise and spanwise wavenumber of the most unstable mode, as predicted by LSA. The resolution is $128 \times 97 \times 96$ and $128 \times 65 \times 96$ in the DNS of XPPF and XPCF, respectively. Figure 11 shows that the DNS and LSA results coincide.

REFERENCES

ALFREDSSON, P.H. & PERSSON, H. 1989 Instabilities in channel flow with system rotation. *J. Fluid Mech.* **202**, 543–557.

ANDERECK, C.D., LIU, S.S. & SWINNEY, H.L. 1986 Flow regimes in a circular Couette system with independently rotating cylinders. *J. Fluid Mech.* **164**, 155–183.

BARLETTA, A. & MULONE, G. 2024 Energy method and stability of shear flows: an elementary tutorial. *Eur. Phys. J. Plus* 139, 906.

BERGHOUT, P., DINGEMANS, R.J., ZHU, X., VERZICCO, R., STEVENS, R.J.A.M., VAN SAARLOOS, W. & LOHSE, D. 2020 Direct numerical simulations of spiral Taylor–Coutte turbulence. *J. Fluid Mech.* 887, A18.

BOECK, T., BRYNJELL-RAHKOLA, M. & DUGUET, Y. 2024 Energy stability of magnetohydrodynamic flow in channels and ducts. J. Fluid Mech. 987, A33.

Brauckmann, H.J., Salewski, M. & Eckhardt, B. 2016 Momentum transport in Taylor–Couette flow with vanishing curvature. *J. Fluid Mech.* **790**, 419–452.

BRETHOUWER, G. 2016 Linear instabilities and recurring bursts of turbulence in rotating channel flow simulations. Phys. Rev. Fluids 1, 054404.

- Brethouwer, G. 2017 Statistics and structure of spanwise rotating turbulent channel flow at moderate Reynolds numbers. *J. Fluid Mech.* 828, 424–458.
- Brethouwer, G. 2019 Influence of spanwise rotation and scalar boundary conditions on passive scalar transport in turbulent channel flow. *Phys. Rev. Fluids* **4**, 014602.
- BRETHOUWER, G. 2021 Much faster heat/mass than momentum transport in rotating Couette flows. J. Fluid Mech. 912, A31.
- Brethouwer, G. 2023 Strong dissimilarity between heat and momentum transfer in rotating Couette flows. *Int. J. Heat Mass Transfer* **205**, 123920.
- Brethouwer, G., Duguet, Y. & Schlatter, P. 2012 Turbulent-laminar coexistence in wall flows with Coriolis, buoyancy or Lorentz forces. *J. Fluid Mech.* **704**, 137–172.
- Brethouwer, G., Schlatter, P., Duguet, Y., Henningson, D.S. & Johansson, A.V. 2014 Recurrent bursts via linear processes in turbulent environments. *Phys. Rev. Lett.* 112, 144502.
- BURIN, M.J. & CZARNOCKI, C.J. 2012 Subcritical transition and spiral turbulence in circular Coutte flow. J. Fluid Mech. 709, 106–122.
- BUSSE, F.H. 1969 Bounds on the transport of mass and momentum by turbulent flow between parallel plates. *Z. Angew. Math. Phys.* **20**, 1–14.
- BUSSE, F.H. 1970 Über notwendige und hinreichende Kriterien für die Stabilität von Strömingen. Z. Angew. Math. Mech. 50, 173–174.
- BUSSE, F.H. 1972 A property of the energy stability limit for plane parallel shear flow. *Arch. Rat. Mech. Anal.* 47 (1), 28–35.
- CHANDRASEKHAR, S. 1961 Hydrodynamic and Hydromagnetic Stability. Oxford University Press.
- CHEVALIER, M., SCHLATTER, P., LUNDBLADH, A. & HENNINGSON, D.S. 2014 A pseudo-spectral solver for incompressible boundary layer flows. KTH Mechanics, Technical Report TRITA-MEK 2007: 07.
- DALY, C.A., SCHNEIDER, T.M., SCHLATTER, P. & PEAKE, N. 2014 Secondary instability and tertiary states in rotating plane Couette flow. *J. Fluid Mech.* **761**, 27–61.
- DAVIAUD, F., HEGSETH, J. & BERGÉ, P. 1992 Subcritical transition to turbulence in plane Couette flow. Phys. Rev. Lett. 69, 2511–2514.
- DUGUET, Y., SCHLATTER, P. & HENNINGSON, D.S. 2010 Formation of turbulent patterns near the onset of transition in plane Couette flow. *J. Fluid Mech.* **650**, 119–129.
- FALSAPERLA, P., GIACOBBE, A. & MULONE, G. 2019 Nonlinear stability results for plane Couette and Poiseuille flows. *Phys. Rev. E* **100**, 013113.
- FINLAY, W.H. 1992 Transition to turbulence in a rotating channel. J. Fluid Mech. 237, 73–99.
- FUENTES, F., GOLUSKIN, D. & CHERNYSHENKO, S. 2022 Global stability of fluid flows despite transient growth of energy. *Phys. Rev. Lett.* **128**, 204502.
- GAI, J., XIA, Z., CAI, Q. & CHEN, S. 2016 Turbulent statistics and flow structures in spanwise-rotating turbulent plane Couette flows. Phys. Rev. Fluids 1, 054401.
- GROSSMANN, S. 2000 The onset of shear flow turbulence. Rev. Mod. Phys. 72, 603-618.
- HART, J.E. 1971 Instability and secondary motion in a rotating channel flow. J. Fluid Mech. 45, 341-351.
- Hu, R., Li, X. & Yu, C. 2023 Multiscale dynamics in streamwise-rotating channel turbulence. J. Fluid Mech. 972, A14.
- Hu, R., Li, X. & Yu, C. 2024 Effects of streamwise rotation on helicity and vortex in channel turbulence. J. Fluid Mech. 980, A50.
- Hung, W.L., Joseph, D.D. & Munson, B.R. 1972 Global stability of spiral flow. Part 2. J. Fluid Mech. 51, 593–612.
- HUNT, J.C., WRAY, A.A. & MOIN, P. 1988 Eddies, Streams, and Convergence Zones in Turbulent Flows. Center for Turbulence Research Report CTR-S88, 193.
- JOSE, S. & GOVINDARAJAN, R. 2020 Non-normal origin of modal instabilities in rotating plane shear flows. Proc. R. Soc. A 476, 20190550.
- Jose, S., Kuzhimparampil, V., Pier, B. & Govindarajan, R. 2017 Algebraic disturbances and their consequences in rotating channel flow transition. *Phys. Rev. Fluids* 2, 083901.
- JOSEPH, D.D. 1966 Nonlinear stability of the Boussinesq equations by the method of energy. *Arch. Rat. Mech. Anal.* 22 (3), 163–184.
- JOSEPH, D.D. 1976 Stability of Fluid Motion I. Springer.
- JOSEPH, D.D. & MUNSON, B.R. 1970 Global stability of spiral flow. J. Fluid Mech. 43, 545–575.
- LEZIUS, D.K. & JOHNSTON, J.P. 1976 Roll-cell instabilities in rotating laminar and turbulent channel flows. *J. Fluid Mech.* 77, 153–176.
- MANNEVILLE, P. 2015 On the transition to turbulence of wall-bounded flows in general, and plane Couette flow in particular. *Eur. J. Mech. B/Fluids* **49**, 345–362.
- MANNEVILLE, P. & ROLLAND, J. 2011 On modelling transitional turbulent flows using under-resolved direct numerical simulations: the case of plane Couette flow. *Theor. Comput. Fluid Dyn.* 25, 407–420.

- MASUDA, S., FUKUDA, S. & NAGATA, M. 2008 Instabilities of plane Poiseuille flow with a streamwise system rotation. *J. Fluid Mech.* **603**, 189–206.
- MESEGUER, A., MELLIBOVSKY, F., AVILA, M. & MARQUES, F. 2009a Families of subcritical spirals in highly counter-rotating Taylor—Couette flow. *Phys. Rev. E* 79, 036309.
- MESEGUER, A., MELLIBOVSKY, F., AVILA, M. & MARQUES, F. 2009b Instability mechanisms and transition scenarios of spiral turbulence in Taylor–Couette flow. *Phys. Rev. E* **80**, 046315.
- NAGATA, M. 1998 Tertiary solutions and their stability in rotating plane Couette flow. *J. Fluid Mech.* **358**, 357–378.
- NAGATA, M., SONG, B. & WALL, D.P. 2021 Onset of vortex structures in rotating plane Couette flow. *J. Fluid Mech.*. 918, A2.
- OBERLACK, M., CABOT, W., REIF, B.A.P. & WELLER, T. 2006 Group analysis, direct numerical simulation and modelling of a turbulent channel flow with streamwise rotation. *J. Fluid Mech.* **562**, 383–403.
- ORR, W.M.F. 1907 The stability or instability of the steady motions of a perfect liquid and of a viscous fluid. Part II: a viscous liquid. *Proc. Roy. Irish Acad. Sect. A: Math. Phys. Sci.* 27, 69–138.
- ORSZAG, S.A. & PATERA, A.T. 1980 Subcritical transition to turbulence in plane channel flows. *Phys. Rev. Lett.* **45**, 989–993.
- PRIGENT, A., GRÉGOIRE, G., CHATÉ, H. & DAUCHOT, O. 2003 Long-wavelength modulation of turbulent shear flows. *Physica D* 174, 100–113.
- RECKTENWALD, I., WELLER, T., SCHRÖDER, W. & OBERLACK, M. 2007 Comparison of direct numerical simulations and particle-image velocimetry data of turbulent channel flow rotating about the streamwise axis. *Phys. Fluids* **19**, 085114.
- REDDY, S.C. & HENNINGSON, D.S. 1993 Energy growth in viscous channel flows. *J. Fluid Mech.* 252, 209–238.
- SALEWSKI, M. & ECKHARDT, B. 2015 Turbulent states in plane Couette flow with rotation. *Phys. Fluids* 27, 045109.
- SCHMID, P.J. & HENNINGSON, D.S. 2001 Stability and transition in shear flows. In *Applied Mathematical Sciences*, vol. 142, Springer.
- SHIMIZU, M. & MANNEVILLE, P. 2019 Bifurcations to turbulence in transitional channel flow. *Phys. Rev. Fluids* **4**, 113903.
- SURYADI, A., SEGALINI, A. & ALFREDSSON, P.H. 2014 Zero absolute vorticity: insight from experiments in rotating laminar plane Couette flow. *Phys. Rev. E* 89, 033003.
- TSUKAHARA, T., TILLMARK, N. & ALFREDSSON, P.H. 2010 Flow regimes in a plane Couette flow with system rotation. *J. Fluid Mech.* **648**, 5–33.
- TUCKERMAN, L., CHANTRY, M. & BARKLEY, D. 2020 Patterns in wall-bounded shear flows. *Annu. Rev. Fluid Mech.* **52**, 343–367.
- WALL, D.P. & NAGATA, M. 2006 Nonlinear secondary flow through a rotating channel. J. Fluid Mech. 564, 25–55.
- WANG, B., AYATS, R., DEGUCHI, K., MELLIBOVSKY, F. & MESEGUER, A. 2022 Self-sustainment of coherent structures in counter-rotating Taylor-Couette flow. *J. Fluid Mech.* **951**, A21.
- WANG, B., MELLIBOVSKY, F., AYATS, R., DEGUCHI, K. & MESEGUER, A. 2023 Mean structure of the supercritical turbulent spiral in Taylor–Couette flow. *Phil. Trans. R. Soc. A* 381, 20220112.
- WU, H. & KASAGI, N. 2004 Effects of arbitrary directional system rotation on turbulent channel flow. *Phys. Fluids* 16, 979–990.
- YANG, K.-S. & KIM, J. 1991 Numerical investigation of instability and transition in rotating plane Poiseuille flow. *Phys. Fluids* 3, 633–641.
- YANG, X.I.A. & XIA, Z. 2021 Bifurcation and multiple states in plane Couette flow with spanwise rotation. J. Fluid Mech. 913, A49.
- YANG, Y.-T., Su, W.-D. & Wu, J.-Z. 2010 Helical-wave decomposition and applications to channel turbulence with streamwise rotation. *J. Fluid Mech.* 662, 91–122.
- YANG, Z., DENG, B.-C., WANG, B.-C. & SHEN, L. 2020 Sustaining mechanism of Taylor-Görtler-like vortices in a streamwise-rotating channel flow. *Phys. Rev. Fluids* 5, 044601.
- YANG, Z. & WANG, B.-C. 2018 Capturing Taylor–Görtler vortices in a streamwise-rotating channel at very high rotation numbers. *J. Fluid Mech.* **838**, 658–689.
- Yu, C., Hu, R., Yan, Z. & Li, X. 2022 Helicity distributions and transfer in turbulent channel flows with streamwise rotation. *J. Fluid Mech.* **940**, A18.